Commun Nonlinear Sci Numer Simulat 149 (2025) 108942

Contents lists available at ScienceDirect

Communications in Nonlinear Science and Numerical Simulation

journal homepage: www.elsevier.com/locate/cnsns

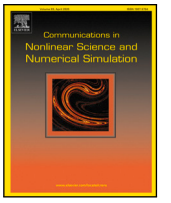

Research paper

Characterization of quasi-periodic dynamics of a magnetic nanoparticle

J.A. Vélez [a,b], L.M. Pérez [c], A.E. Pizarro [d], L. Pedraja-Rejas [c], O.J. Suarez [e], R. Hernández-García [f,g], R.J. Barrientos [f,d], J. Bragard [h,i,*], D. Laroze [j], R.M. Otxoa [k,a]

[a] Donostia International Physics Center, 20018 San Sebastián, Spain
[b] Polymers and Advanced Materials Department: Physics, Chemistry, and Technology, University of the Basque Country, UPV/EHU, 20018 San Sebastián, Spain
[c] Departamento de Ingeniería Industrial y de Sistemas, Universidad de Tarapacá, Casilla 7D, Arica, Chile
[d] DCI Department, Faculty of Engineering Sciences, Universidad Católica del Maule, 3480112 Talca, Chile
[e] Departamento de Física, Universidad de Sucre, A.A. 406, Sincelejo, Colombia
[f] Laboratory of Technological Research in Pattern Recognition (LITRP), Universidad Católica del Maule, 3480112 Talca, Chile
[g] Research Center for Advanced Studies of Maule (CIEAM), Universidad Católica del Maule, 3480112 Talca, Chile
[h] Departamento de Física y Matemática Aplicada, Universidad de Navarra, 31080, Pamplona, Spain
[i] Instituto de Ciencia de los Datos e Inteligencia Artificial, Universidad de Navarra, 31080, Pamplona, Spain
[j] Instituto de Alta Investigación, Universidad de Tarapacá, Casilla 7D, Arica, Chile
[k] Hitachi Cambridge Laboratory, J. J. Thomson Avenue, Cambridge CB3 0HE, United Kingdom

ARTICLE INFO

Keywords:
Magnetization dynamics
Lyapunov exponents
Quasi-periodic behavior
Chaos

ABSTRACT

This work presents a systematic characterization of the quasi-periodic dynamics of a uniaxial anisotropic magnetic nanoparticle under the influence of a time-varying external magnetic field. Using the Landau–Lifshitz–Gilbert (LLG) formalism, we analyze the response of the system as a function of key parameters, particularly focusing on the effects of magnetic anisotropy and dissipation. Through an extensive numerical exploration, we identify transitions between periodic, quasi-periodic, and chaotic regimes, employing Lyapunov exponents, isospike diagrams, Fourier spectra, and winding number calculations. The results reveal that the anisotropy parameter strongly influences the asymmetry of the dynamical states, leading to distinct behaviors along the easy and hard anisotropy axes. Additionally, at low dissipation, direct transitions between quasi-periodic and chaotic states emerge as a function of the external field, while at higher dissipation, periodic states dominate. The winding number analysis uncovers complex hierarchical structures, including self-similar step-like formations characteristic of the so-called Devil's staircase phenomenon, along with a granular transition mechanism between quasi-periodic and chaotic states. Furthermore, the role of initial conditions is explored, demonstrating the presence of multistability, where different attractors coexist depending on the initial configuration. These results contribute to a deeper understanding of the nonlinear magnetization dynamics in anisotropic nanoparticles and may serve as a reference for future studies exploring the influence of quasi-periodic behavior in spintronic systems.

* Corresponding author.
E-mail address: jbragard@unav.es (J. Bragard).

https://doi.org/10.1016/j.cnsns.2025.108942
Received 21 October 2024; Received in revised form 6 March 2025; Accepted 4 May 2025
Available online 22 May 2025

1. Introduction

The study of nonlinear and complex systems has a long-standing tradition in both natural and social sciences. In physics, it encompasses systems at every length scale, demonstrating its broad applicability. Modern spin-based devices composed of small ferromagnets and/or antiferromagnets are fundamental components in current spintronic applications. Nano- and micrometric structures exhibit essential features from both technological and fundamental perspectives due to their rich and non-trivial dynamics. Recent advances in nanopatterning techniques have enabled the fabrication of magnetic nanostructures with specific operational properties. The dynamics associated with nanomagnetic systems are highly diverse, including switching, self-sustained oscillations, synchronization, and chaotic behavior. Two primary excitation protocols can induce these dynamics: (i) the application of an external magnetic field, which generates a torque on the magnetization, and (ii) the transfer of spin angular momentum from conducting electrons to the local magnetization. This spin-polarized current can also exert a torque on the magnetization, commonly referred to as spin-transfer torque. At a length scale ranging from hundreds of nanometers to several microns, a classical approach to describing magnetization dynamics under an external force is the well-known Landau–Lifshitz–Gilbert (LLG) equation [1–4]. The present study employs the LLG equation to investigate the dynamics of a magnetic system. In the case of nanoparticles, the justification for this approach stems from the assumption that spatial inhomogeneities can be neglected, and the monodomain limit is commonly used [3]. Recent advances in nonlinear magnetization dynamics research are extensive and can be found in the following Refs. [5–45], but many open questions remain unresolved.

In natural systems exhibiting two or more interacting frequencies and nonlinearity, various intriguing dynamics can emerge, including frequency locking, quasi-periodicity, intermittency, subharmonic generation, and chaos. Quasi-periodic behavior is a distinct type of dynamics characterized by a finite number of incommensurable frequencies (usually two or three). These frequencies can be approximated in Fourier space, while in real space, the trajectory densely covers a torus [46]. The dimensionality of the torus corresponds to the number of independent frequencies in the system. Moreover, quasi-periodicity often serves as a precursor state to chaotic dynamics. Specifically, a three-dimensional torus is generally unstable and transitions into chaos, as described in the Ruelle-Takens [47] route to chaos. Several studies, both experimental and theoretical, have explored quasi-periodic routes to chaos and quasiperiodicity. Notable works include [48–60]. In particular, quasi-periodicity has been observed in celestial mechanics, nonlinear wave solutions, and localized structures. Furthermore, quasi-periodic behavior has been identified in magnetization dynamics [61–64]. Experimental studies have demonstrated commensurability effects and chaotic transitions in nanoscale magnetic vortex oscillators, highlighting the presence of Devil's staircase structures and phase-locked states [65]. However, to the best of our knowledge, a systematic characterization of these states within the framework of the LLG equation remains unexplored.

The primary objective of this paper is to conduct a systematic and detailed characterization of quasi-periodic dynamics in magnetic nanoparticles, a subject that has not been explored at this level of precision. We analyze the response of a magnetic system subjected to a time-varying external magnetic field governed by the LLG equation. Specifically, we perform a numerical study of periodic driving in the direction perpendicular to the anisotropy axis, known as the easy axis. The study employs advanced nonlinear dynamics tools, including Lyapunov exponents (LEs), isospike diagrams, Fourier spectra, and winding number calculations, to thoroughly explore the parameter space and construct two-dimensional phase diagrams that delineate periodic, quasi-periodic, and chaotic regimes. This investigation provides an in-depth classification of quasi-periodic states, with a particular focus on the torus T^2 and the fundamental phenomenon of phase locking, which arises when the ratio of two incommensurable frequencies becomes rational. This effect is of great technological significance and is extensively analyzed in this paper. Furthermore, the computational aspects of winding number calculations are discussed. The influence of dissipation and the amplitude of the applied field on quasi-periodic states is examined in detail. To ensure the accuracy of our calculations, different methods for computing the winding number are presented in an Appendix, achieving a precision of at least 10^{-5}. Finally, we analyze the effect of initial conditions on the selected dynamical states, revealing the presence of multistability within the basin of attraction. Since the dynamics of nonlinear magnetic systems play a crucial role in the control and stability of spin–torque oscillators, our results provide a theoretical foundation for optimizing these systems in advanced technological applications. In particular, the sensitivity to initial conditions and the structure of attractors can be exploited to improve information processing and transmission in spintronic devices, where quasi-periodic dynamics and multistability could be utilized as functional resources in emerging computing architectures [66–76].

The structure of this paper is as follows. In Section 2, we present the theoretical model describing the magnetization dynamics of a uniaxial anisotropic nanoparticle, based on the Landau–Lifshitz–Gilbert (LLG) equation. We provide details on the governing equations, the external driving field, and the relevant material parameters. In Section 3, we conduct a comprehensive numerical analysis, systematically exploring the impact of anisotropy, damping, and external field strength on the dynamical states of the system. We characterize the transitions between periodic, quasi-periodic, and chaotic regimes using various dynamical indicators, such as Lyapunov exponents, isospike diagrams, and winding number computations. Additionally, we investigate the role of initial conditions and analyze the multi-stability of the system. Finally, in Section 4, we summarize our main findings, discuss their implications in magnetic applications on neuromorphic computing, and outline possible future research directions.

2. Model for the magnetization of a nanoparticle

The system under consideration corresponds to a magnetic nanoparticle which represents a magnetic monodomain with magnetization, **M**. The temporal evolution of magnetization dynamics is described by the LLG equation, which in its explicit form is [1,2]:

$$\frac{d\mathbf{M}}{dt} = -\frac{\gamma}{1+\eta^2}\mathbf{M}\times\mathbf{\Gamma} - \frac{\eta\gamma}{(1+\eta^2)M_S}\mathbf{M}\times(\mathbf{M}\times\mathbf{\Gamma}), \tag{1}$$

Table 1
Experimental values of the anisotropy constant (K_{u1}), saturation magnetization (M_S), corresponding dimensionless damping parameter (η), and β_z for various uniaxial materials. These values serve as a reference for the parameter space explored in our numerical simulations. Data for K_{u1}, M_S, and β_z taken from Ref. [79]. The values of η are taken from Refs. [80–82].

Materials	$K_{u1}(10^3$ J/m$^3)$	$M_S(10^6$ A/m)	β_z	η
$Ni_{80}Fe_{20}$	0.15	0.84	3.3×10^{-4}	0.0048–0.0144
Fe	48	1.71	0.026	0.0020–0.0050
Co	410	1.44	0.314	0.0101–0.0417
CoPt	4900	0.81	11.88	0.0526–0.1111
Fe_3O_4	−13	0.48	−0.09	0.0204–0.0309
CrO_2	25	0.39	0.26	~ 0.001

where γ is the gyromagnetic factor, which is associated with the electron spin and whose numerical value is approximately given by $\gamma = |\gamma_e|\mu_0 \approx 2.21\times10^5$ m A^{-1}s^{-1}. Here, η stands for the phenomenological dimensionless damping constant, known as the Gilbert damping constant. The effective magnetic field, $\mathbf{\Gamma}$ contains all effects both from external and internal fields or energy contributions. The LLG equation describes the precessional motion of the magnetization around the effective magnetic field. Analytic solutions of the LLG equation have been obtained in the so-called macro-spin approximation [1,4], which is only valid for situations where the size of the magnetic particle is larger than 10 nm [77,78]. Let us comment that an experimental value of the saturation magnetization is, for example, $M_{s[\mathrm{Co}]} \approx 1.42\times10^6$ A/m ≈ 17.8 kOe for cobalt-based materials, implying that the time scale is $(|\gamma|M_{s[\mathrm{Co}]})^{-1} \approx 3$ ps [3].

The effective field, $\mathbf{\Gamma}$, for a uniaxial anisotropic nanoparticle is given by:

$$\mathbf{\Gamma} = \mathbf{H} + \beta_n\,(\mathbf{M}\cdot\hat{\mathbf{n}})\,\hat{\mathbf{n}}, \tag{2}$$

where $\mathbf{H}$ is the external magnetic field and β_n measures the anisotropy along the $\mathbf{n}$ axis. We remark here that we do not consider dipolar and exchange interactions as in our scenario a single magnetic moment is considered. We apply an external magnetic field $\mathbf{H}$ that comprises both, a constant longitudinal field, $\mathbf{H}_0(\|\hat{\boldsymbol{z}})$ and parallel to the anisotropy direction, $\hat{\mathbf{n}}$, and a perpendicular component ($\perp\hat{\boldsymbol{z}}$) with fixed amplitude and frequency:

$$\mathbf{H} = \mathbf{H}_0 + \mathbf{H}_T\sin(\omega t), \tag{3}$$

where both $\mathbf{H}_0 = H_z\hat{z}$ and $\mathbf{H}_T = H_x\hat{x} + H_y\hat{y}$ are time-independent. For this model, no relevant changes are obtained due to the phase of the applied external magnetic field [43]. We assume that the particle is fixed with the anisotropy axis along the constant field, $\mathbf{n}\|\hat{\mathbf{z}}$, and only the magnetization $\mathbf{M}$ is rotating. The dissipation and the oscillatory injection of energy move the magnetic particle into an out-of-equilibrium situation. In such a circumstance, the magnetization of the particle may exhibit complex behaviors [35,61]. In this work, we will focus mainly on the dissipation effect, which will be analyzed in the next section.

To contextualize the range of anisotropy values used in this study, we present in Table 1 experimental values of the anisotropy constant (K_{u1}), saturation magnetization (M_S), and the corresponding normalized anisotropy parameter (β_z) for several uniaxial materials. The parameter β_z is computed as:

$$\beta_z = \frac{K_{u1}}{\mu_0 M_S^2}, \tag{4}$$

where μ_0 is the vacuum permeability. These values serve as a reference to compare with the parameter ranges explored in our numerical simulations.

3. Numerical results

This section is divided into four parts. In the first subsection, we present a brief description of the dynamical indicators used to characterize the dynamics. In the second subsection, we show and analyze the numerical simulations taking into account the intrinsic material parameters, that means the anisotropy and the dissipation. In the third subsection, we present the results associated with the amplitude of the applied time-varying external magnetic field and the damping parameter. Finally, we analyze the effect of the initial conditions on the dynamical states.

3.1. Dynamical indicators

The dynamical states are characterized using mainly two techniques; Lyapunov exponents and the computation of the isospike. The bifurcation diagrams, and Fourier transforms, and winding number are also used as complementary indicators to describe specific states. These methods have been extensively used to characterize the dynamical states of several nonlinear systems [83–114]. Let us also remark that we consider the dimensionless and normalized LLG equation for the external applied field, the magnetic moment, time and frequency given by: $\mathbf{h} = \mathbf{H}/M_s$, $\mathbf{m} = \mathbf{M}/M_s$, $\tau = t\gamma M_s$ and $\Omega = \omega/\gamma M_s$, respectively. Note that for this normalization, we obtain $|\mathbf{m}| = 1$. The LLG equation contains a periodic forcing term with an explicit time dependence, therefore, the dynamics corresponds to a non-autonomous system. We aggregate a new variable Σ to the description of the dynamical system

by applying a transformation of the form: $\Sigma = \Omega\tau$. This leads to a dynamical system that contains an additional differential equation for the new variable $d\Sigma/d\tau = \Omega$. By doing this mathematical procedure, the system becomes now autonomous in four dimensions. Nevertheless, due to the conservation of the norm, i.e., $|\mathbf{m}| = 1$, the system is effectively three-dimensional.

One of the principal indicators for discriminating chaotic behaviors are the Lyapunov exponents (LEs) where, we refer to chaos by the huge sensitivity to the initial conditions for a given system. The LEs quantify the mean divergence of two initially closed trajectories. LEs are extensively used to determine whether the dynamical regime corresponds to chaotic **C**, periodic **P**, or quasi-periodic **QP**. We denote the LEs by λ_i after they are sorted in descending order $\lambda_1 > \lambda_2 > \cdots \lambda_N$. We remark here that the introduction of an additional differential equation to render the system autonomous implies that we always get $\lambda_2 = 0$. The chaotic states, **C**, correspond to $\lambda_1 > 0$. The quasi-periodic states, (**QP**), are present when $\lambda_1 = \lambda_2 = \lambda_3 = 0$. Finally, the periodic states, (**P**), are obtained provided $\lambda_1 = \lambda_2 = 0$ and $\lambda_3 < 0$ [83,84]. Let us remark here that as we have a low-dimensional dissipative system, there is no option to observe quasi-periodic states with three frequencies. This rules out, in the present system, the transition from a T^3-torus to chaos as it was discovered by Ruelle and Takens [47].

Additional information about the dynamics is obtained through the isospike computations, which provide insights into the convolutions of periodic orbits in the phase space. In practice, the isospike is calculated for each component of the time series by counting the number of local maxima within a period. For a periodic signal, three positive integers corresponding to the isospike values of the three components of the magnetization vector are computed. The advantage of this method is that it allows for qualitative differentiation between periodic solutions with distinct structures and helps to identify regions of chaotic (**C**), quasi-periodic (**QP**), and periodic (**P**) states. This process is performed using an algorithm that adapts the classification according to the type of periodicity detected. When the time series does not exhibit a clearly regular pattern, the algorithm discards the classification as a **P** state and assigns it to **C** or **QP** accordingly. These diagrams are displayed with a color bar code. In which, each number of spike per period is represented by a specific color. Additionally, in the isospike diagrams, values labeled as ≥ 17 in the color bar simply indicate that the number of peaks in the time series is greater than 17. This value does not imply that these states are chaotic or quasi-periodic; rather, it corresponds to periodic solutions with high isospike number within the set of regular states (**P**).

Let us comment that, while the computation of the LE requires heavy computational numerics, the computation of the isospikes is rather straightforward and could be done with a rather short time series. One of the advantages of isospike diagrams is that they can also be implemented to work with experimental data. Moreover, in order to extract the period of the dynamics of the magnetization vector, we calculate the Fourier transform of each component of **m**, and estimate the oscillating period from the Fourier spectra. Additionally, phase diagrams, time series, and bifurcation diagrams over the m_x-component are also extracted to discriminate chaotic states.

On the other hand, in order to explore more thoroughly the transitions between the periodic, **QP** and chaotic states, we computed the winding number associated with the dynamics. To provide a precise description of this quantity, we first recall its definition and significance in dynamical systems.

Quasi-periodicity is observed in many dynamical systems, and as it is well known, in some instances, the quasi-periodic states can lock in a periodic state through a synchronization process. This process can be internally or externally driven. The method of choice for studying **QP** is the method developed by Poincaré at the turn of the twentieth century. If the dynamic manifold consists of a torus T^2, a stroboscopic view taken at times $\tau_1 = 1/\mathcal{F}_1$ will define a Poincaré section. In this case, the section will be either a finite set of discrete points or a quasi-continuous curve. The trajectory in the Poincaré section provides a geometric representation of the system's underlying frequency relations, allowing us to distinguish between periodic and quasi-periodic motion. The dynamics in the Poincaré section is dictated by the second characteristic time $\tau_2 = 1/\mathcal{F}_2$, associated with the second frequency of the system. One distinguishes two cases: if the frequency ratio $\mathcal{F}_2/\mathcal{F}_1$ is rational, we indeed have a periodic system, and the system is locked in (mode locking). On the contrary, if the frequency ratio $\mathcal{F}_2/\mathcal{F}_1$ is irrational, the system is in a true **QP** dynamics, and the dynamics draws a quasi-continuous curve on the Poincaré section. This distinction is essential in understanding the transition from quasi-periodic to periodic behavior, which plays a fundamental role in nonlinear dynamics. Another useful technique to evaluate the winding number is to look for a Lissajous pattern [51].

To systematically differentiate these cases, the winding number is computed. The easy way to distinguish these two cases is to calculate the winding number. Suppose one can define an unequivocal phase θ, determining the angular locations of the successive points in the Poincaré section. In that case, the winding number $\mathcal{W}$ is defined as follows:

$$\mathcal{W} = \lim_{i\to\infty} \frac{\theta_i - \theta_0}{2\pi i} \,, \tag{5}$$

where in the above formula, i indicates the iteration number on the Poincaré section, and $\theta_i \in \mathcal{R}$ is the unfolded phase angle after i iterations. The computation of the winding number is illustrated in Appendix A. To ensure an accurate evaluation of the winding number, we perform long-time simulations spanning $\tau = 2\times 10^5$, collecting approximately 3.183×10^4 stroboscopic data points. The main fundamental frequency $\mathcal{F}_1$ value is given by $\mathcal{F}_1 = 1/(2\pi)$.

3.2. Numerical procedure

Let us comment on the numerical procedure regarding the simulation of the LLE equation. The numerical integration of the dynamical system is performed using the standard fourth-order Runge–Kutta (RK4) method with a fixed time step of $d\tau = 0.001$. Additionally, we have integrated the dynamics using a recently introduced pseudo-symplectic method [115,116]. A detailed comparison between these two numerical schemes is provided in Appendix B, where we demonstrate that, despite not being symplectic, the RK4 method achieves sufficient accuracy for the present analysis. Furthermore, the conservation of the magnetization

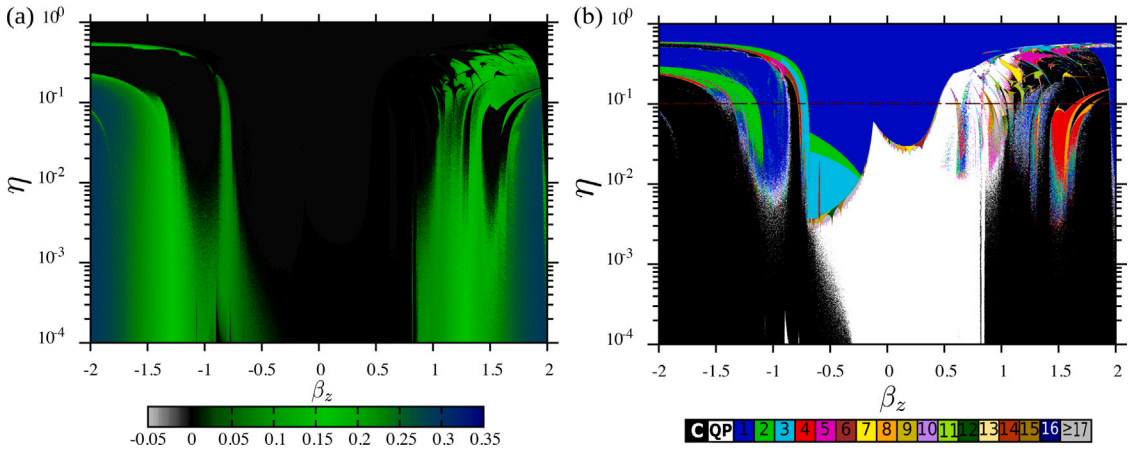

Fig. 1. Phase diagrams in color code as a function of the damping η (vertical axis) and the anisotropy parameter β_z (horizontal axis). The left panel (a) shows the largest Lyapunov exponent, while the right panel (b) displays the isospike diagram for the magnetization component m_x. The fixed parameters are: $\Omega = 1.0$, $h_x = 1.0$, $h_y = 0$, and $h_z = 0.10$. The initial conditions for all simulations are set to $m_x = 0.1$, $m_y = 0.1$, and $m_z = -\sqrt{1 - m_x^2 - m_y^2}$ to ensure normalization of the magnetization vector.

modulus and the consistency of the numerical results have been validated through a direct comparison with the pseudo-symplectic integrator. To study the steady-state dynamics, a transient period of $\tau_{\text{trans}} = 50000$ is always discarded before conducting the analysis. The Lyapunov exponent (LE) computation is performed by evaluating the divergence of trajectories over a time interval of $\tau_{\text{LE}} = 10000$. The isospike diagram is obtained by analyzing the local maxima and minima of the time series over a period of $\tau_{\text{iso}} = 10000$, recorded after τ_{LE}. This extended observation time, $\tau_{\text{iso}} = 10000$, is chosen because the signal frequency is not known a priori, and its estimation is performed in parallel with the isospike computation.

3.3. Damping and anisotropy effects

In this subsection, we analyzed the effect of the materials parameters (the anisotropy coefficient and the damping constant) in a wide range of fixed driving frequency and field amplitude values. It is motivated because different magnetic materials give a variety of values. For instance, the orders of magnitude of α are 10^{-4} to 10^{-3} in garnets; or 10^{-2} or greater for cobalt, nickel or permalloy ($Ni_{80}Fe_{20}$) [3]. In the case of the anisotropy constant, it can even change sign. Some experimental values of the anisotropy parameter and their corresponding β_z are given in Table 1. These values serve as a reference for the parameter space explored in our numerical simulations.

The left panel of Fig. 1a displays the largest LE, (λ_1), in color code as a function of the material parameters η in logarithmic scale and the anisotropy β_z (horizontal axis). These two material properties have a drastic importance in modifying the dynamics of the system.

In the specific case displayed in Fig. 1, one observes from the left panel of Fig. 1, that for values of β_z in the range between -0.5 and 0.7 there are very few chaotic dynamical states. Fig. 1b reveals that in the same range of values β_z, the system exhibits periodic **P** and **QP** states. For lower values of the damping ($\eta < 10^{-2}$), the **QP** states prevail with some small area of **C** near $\beta_z = -0.5$ and $\eta < 10^{-3}$. In Fig. 1b for η close to 1, one can see a periodic signal with an isospike count of one for the m_x-component. It is worth recalling that the quantity of peaks that are shown in the isospike counts depends upon the component that one is considering, as it will become clear in the analysis of later figures.

In Fig. 1b, for $\eta > 10^{-2}$ and $\beta_z > 0.7$, we observe different periodicity islands surrounded by chaotic regions. This behavior resembles the classical periodic windows embedded in the logistic map. The additional information provided here with the isospike computation is that the periodic windows have their own characteristic structure indicated by the isospike counts. For $\eta < 10^{-2}$ and $\beta_z > 0.7$, the dissipation is reduced, and the system exhibits only chaotic states. On the other hand, for $\eta < 10^{-2}$ and $\beta_z < -0.5$, the dynamics is mainly chaotic with tiny windows of **QP** near $\beta = -1$. This highlights the crucial role of the anisotropy parameter in determining the dynamical state. For $\eta > 10^{-0.8}$ and $\beta_z < -1.5$, we observe a transition between **C** and **P** states rather well defined. To analyze the different bifurcations occurring in the system, we select a specific value of $\eta = 10^{-1}$, indicated by the white dashed horizontal line in Fig. 1b.

Fig. 2 shows the bifurcation diagram and the LEs associated with the specific value of $\eta = 10^{-1}$ as indicated in Fig. 1b. The top panel of Fig. 2 shows the values of the m_x-component obtained from a Poincaré section of the dynamics. It can be observed that almost all values of m_x are densely populated in the **C** state, whereas the **P** states exhibit well-defined discrete values corresponding to the isospike count. The **QP** states in the bifurcation diagram are intermediate states between chaotic and periodic regimes, where the dispersion of the points is constrained to bounded regions that expand as the parameter β_z varies.

The bottom part of the panel of Fig. 2b shows a color stripe that classifies the dynamical state. Red color is used for **C** states, gray for **P** states and green for **QP** states. One can observe that for the green stripes (**QP** states) one gets that λ_1 and λ_3 are vanishing.

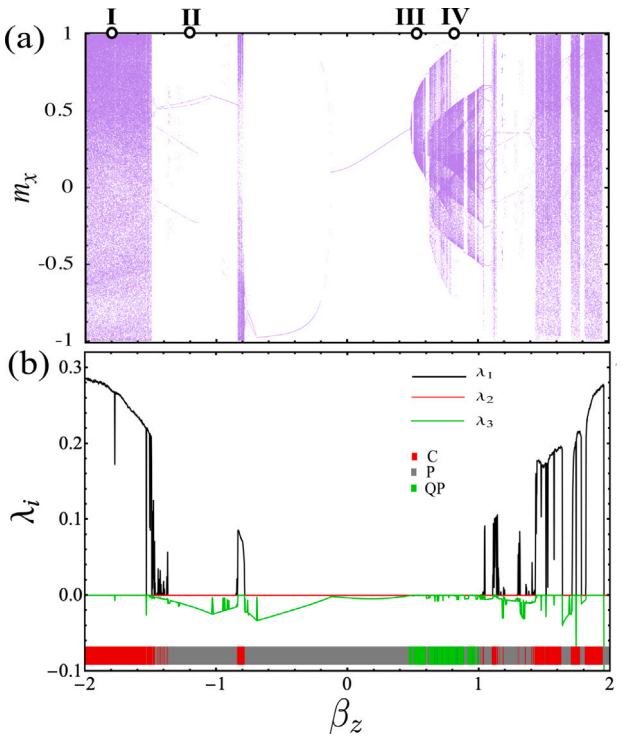

Fig. 2. Panel (a) presents the bifurcation diagram obtained using the m_x component. Panel (b) shows the first three Lyapunov exponents as a function of β_z. Both panels correspond to the dashed line for $\eta = 0.1$, as indicated in Fig. 1. The color bar below panel (b) classifies the dynamical states as chaotic (**C**, red), periodic (**P**, gray), and quasi-periodic (**QP**, green). The fixed parameters and initial conditions are the same as in Fig. 1.

There is an interesting mix between **P** and **QP** states which occurs for β_z in the range between 0.5 and 1. Additionally, the transition to chaotic states always originates from purely periodic states, following a periodic route to chaos, rather than from **QP** states. In the top of the panel in Fig. 2a we have selected four points: **I**, **II**, **III** *y* **IV**, which correspond to specific cases shown in Fig. 3. The case **I** corresponds to a chaotic; case **II** is periodic, and **III** and **IV** are **QP** states with different polarization along the $\hat{z}$-axis.

Fig. 3 displays the dynamical information of the four selected cases. The first column, panels (a, d, g, j) show the trajectory of the dynamics in the three dimensional phase space. The second column, corresponding to the panels (b, e, h, k) show the time series of the m_x-component. The third column of Fig. 3, corresponding to the panels (c, f, i, l) display the Fourier spectra of the m_y-component. In the panel 3a for $\beta_z = -1.8$, one can observe that in the chaotic case, the magnetic moment covers the whole sphere $|\mathbf{m}|^2 = 1$ with a trajectory that does not follow a regular pattern. This is reflected in Fig. 3c, where the Fourier spectrum reveals a characteristic broad band structure that is typical of the **C** states. In the specific case **II** for $\beta_z = -1.2$, we observe a periodic state with two isospikes (two local maxima for each period of the signal). The Fourier spectrum, panel 3f shows peaks with very precise frequencies which follow the distribution given by: $\mathcal{F} \subset \{\mathcal{F}_0, 2\mathcal{F}_0, 3\mathcal{F}_0, \ldots\}$, where $\mathcal{F}_0$ is the main oscillating frequency and its numerical value is approximately given by $\mathcal{F}_0 = 0.084$. For a typical cobalt material, this corresponds to an approximate frequency of $f \approx 28$ GHz.

The points corresponding to cases **III**, for $\beta_z = 0.55$ and **IV** $\beta_z = 0.8$ are in the **QP** states. The dynamics shown in panels (3g, 3j) contain very tightly closed trajectories which open up slowly but do not exhibit sensibility to initial conditions. The Fourier spectra show peaks that are given by: $\mathcal{F} \subset \{m_1\mathcal{F}_1, m_2\mathcal{F}_2\}$, where $\mathcal{F}_1$ and $\mathcal{F}_2$ are the two dominant frequencies and m_1 and m_2 are small integers. It is relatively easy to identify the secondary peaks of the Fourier spectrum by their associated m_1 and m_2 numbers. In practice, this identification requires solving a simple linear Diophantine equation to determine m_1 and m_2 for each dominant peak in the Fourier spectrum. In the case of a true **QP** state, the ratio $\mathcal{F}_1/\mathcal{F}_2$ is irrational and by invoking the Bézout's lemma, one can be assured to find a solution to the aforementioned Diophantine equations [117].

Note that in practice, due to the finite precision of the computation of the Fourier spectra, one only needs to check that the integer indices corresponding to the dominant peaks $\mathcal{F}_1$ and $\mathcal{F}_2$ are co-primes. From a physical perspective, the dynamical regimes **III** and **IV** show that the system undergoes a magnetization reversal by means of **QP** trajectories. This behavior is typical for magnetic systems which are forced periodically.

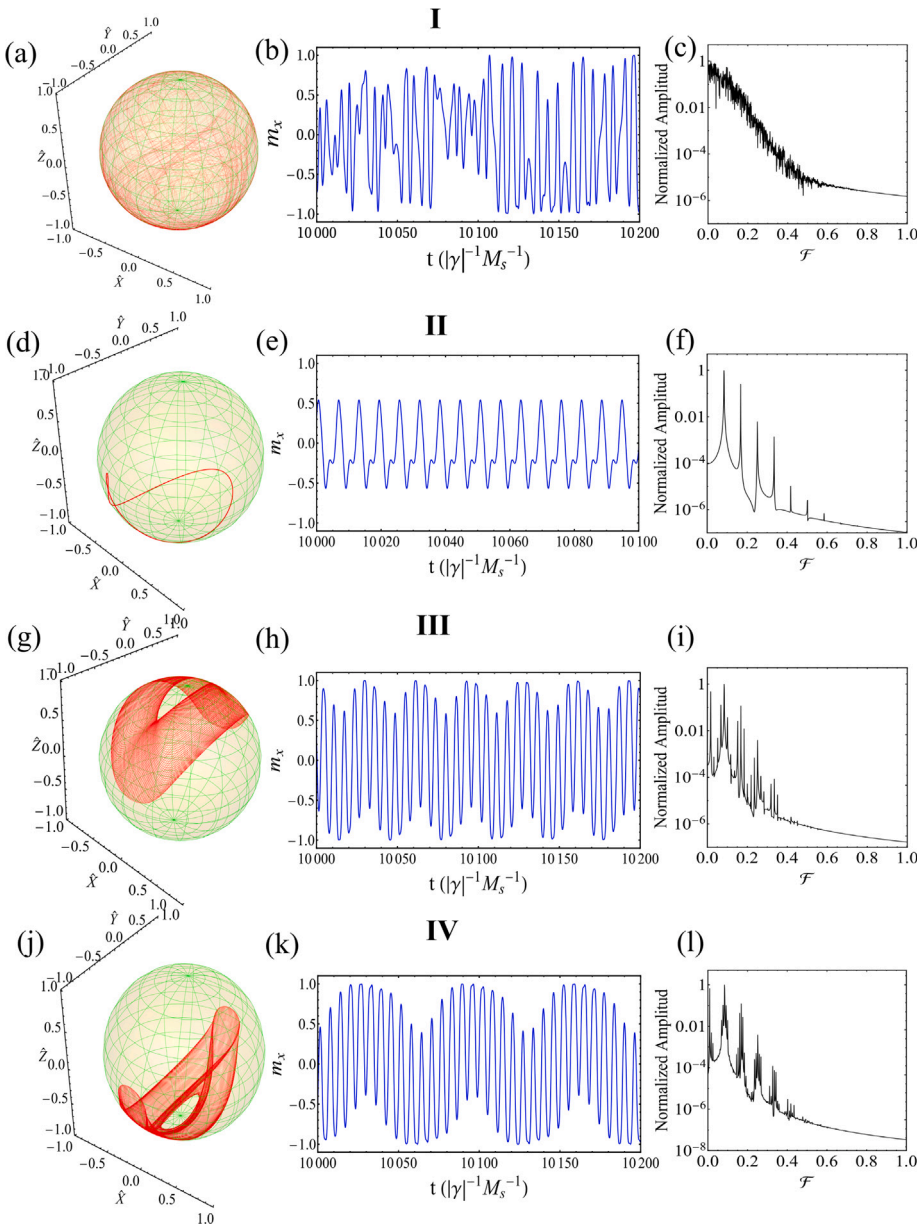

Fig. 3. Four typical cases of the dynamics. The rows correspond to cases **I** to **IV**, with parameter values $\beta_z = [-1.8, -1.2, 0.55, 0.8]$. The columns represent, respectively, the trajectories in phase space, the time series of m_x, and the Fourier transform. The fixed parameters and initial conditions are the same as those in Figs. 1 and 2.

3.4. Combined effect of damping and applied field's amplitude

In this section, we propose to analyze the combined effect of the damping coefficient η and the magnitude of the applied field h_x on the magnetization dynamics. As expected, both parameters play a crucial role in determining the dominant dynamical regimes. We systematically explore the parameter space η and h_x.

A summary of the results is presented in Figs. 4a-4d. Figs. 4a-4c show the isospike diagrams for the three components of the magnetization, i.e., the m_x, m_{xy}, and m_z components. Fig. 4d displays the period of the periodic signals expressed in dimensionless time units.

From Figs. 4a-4c, one observes that the number of isospikes for a given set of parameters varies depending on the specific magnetization component analyzed. The isospike panels in Figs. 4a-4c highlight the crucial role of the external magnetic field, h_x, in shaping the dynamical structures of the system.

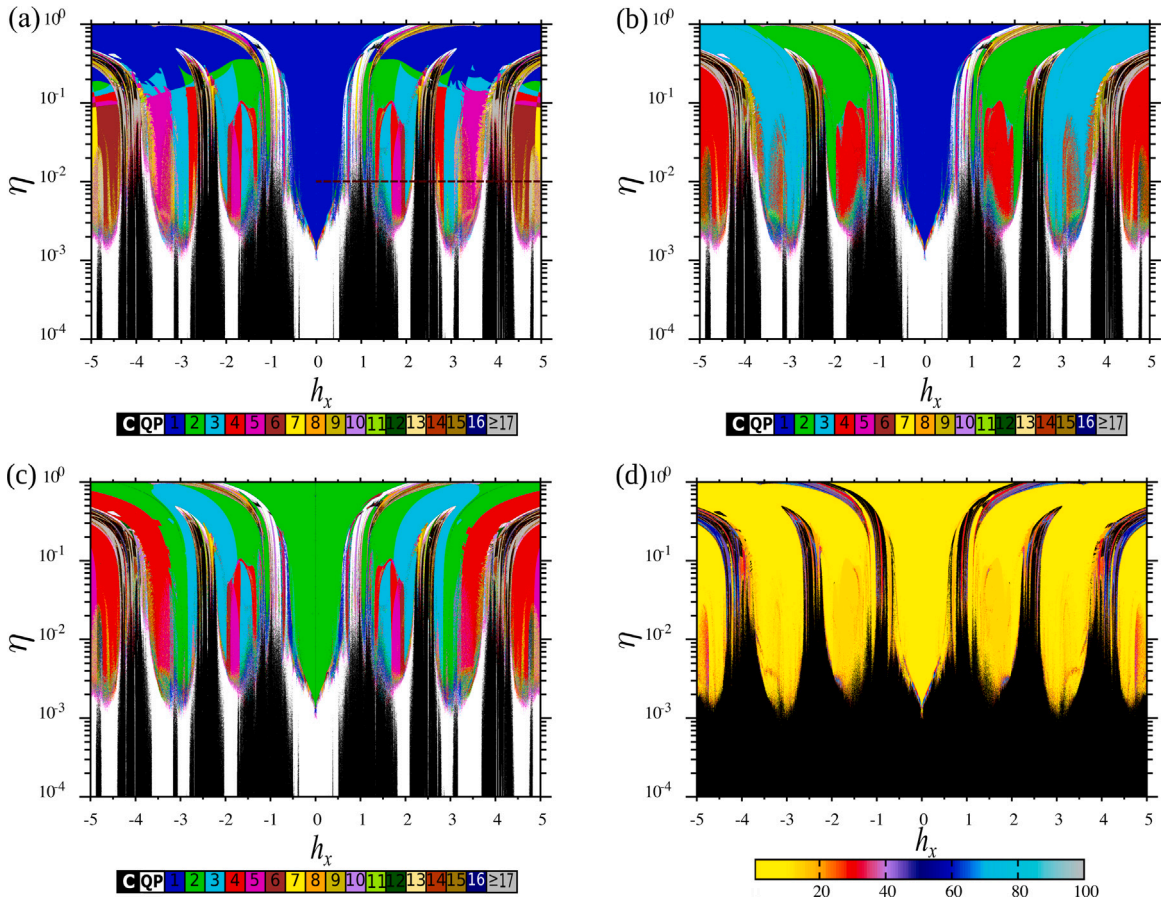

Fig. 4. Phase diagrams in color code as a function of the damping η and the driven field amplitude h_x. Panels (a), (b), and (c) correspond to the isospike diagrams for the magnetization components (m_x, m_y, m_z), respectively, while panel (d) represents the periodic distribution. The fixed parameters are: $\Omega = 1.0$, $h_y = 0.0$, $h_z = 0.1$, and $\beta_z = 1.0$. The initial conditions are set to $m_x = 0.1$, $m_y = 0.1$, and $m_z = -\sqrt{1 - m_x^2 - m_y^2}$.

Again, it is worth noting that **QP** and **C** states appear for low values of the damping coefficient $\eta < 10^{-2}$, with notable phase transitions between **QP** and **C** states as h_x is varied. This is reminiscent of the quasi-periodicity route toward chaos [46].

For the periodic states, in Fig. 4a, we observe that the m_x-component for $\eta > 10^{-0.8}$ contains essentially a single peak in the time series, as indicated by an isospike count of one. Conversely, for the m_y and m_z-components, as shown in Figs. 4b, 4c, multiple peaks are observed in the isospike diagrams, corresponding to different periodicity structures.

An increase of the damping parameter η shows that the transitions observed when varying the parameter h_x are now between **QP** and **P** states. Specifically, for a fixed value of $h_x = 3$, we observe that an increase of η transforms the **QP** state into a diffuse state of **P** states. This behavior resembles mode-locking phenomena observed in transitions between **QP** and **P** states. These diffuse **P** states are presumably Arnold's tongues that are intermingled with **QP** states [51].

The same sort of transition also happens between **C** and **P** states. Indeed in Fig. 4c, for a fixed value of $h_x = -1.5$, we observe that an increase of η transforms the **C** state into a diffuse state of **P** states. This observation aligns with the periodic route to chaos [46].

Fig. 4d provides a visualization of the time period distribution (in dimensionless time units) as we vary the two parameters η and h_x. The most common period is indicated by the yellow color and corresponds to a period of 2π time unit. The color changes in Fig. 4d represent transitions to longer dominant periods, reminiscent of bifurcation (Hopf bifurcation) associated with period doubling as a precursor to chaotic behavior [46]. In our simulations, periods exceeding 60 time units were rarely observed. Note that Fig. 4d was constructed using the dominant peak in the Fourier spectrum to approximate the dominant period when the system is not chaotic. These diagrams do not allow us to distinguish between **QP** and **C** states.

The panel (a) of Fig. 5 shows the corresponding LEs as a function of the parameter h_x in the range between 0 and 5 along a cut in Fig. 4a for a fixed value of the parameter $\eta = 0.01$. The colored bar in the bottom part in panel (a) Fig. 5 classifies the states according to their LE. For values of $h_x = [0, 1]$, one sees many transitions between **P** and **QP** states, again indicating locking between periodic states embedded within a **QP** dynamics [46]. For $2.2 < h_x < 2.7$ a chaotic window with many transitions between **P**, **QP** and **C** are observed.

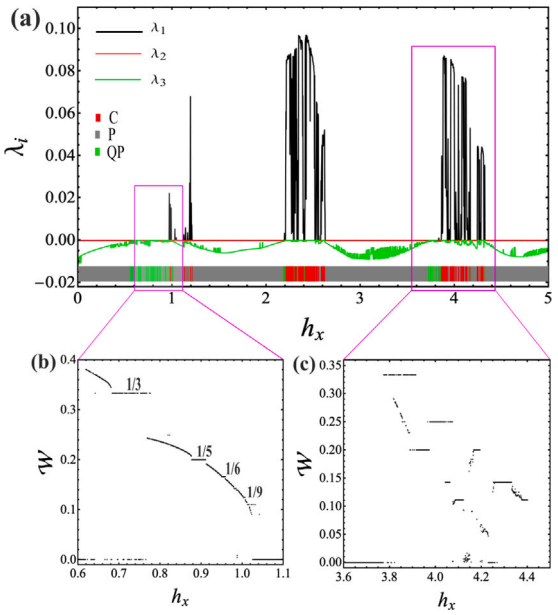

Fig. 5. Panel (a) shows the first three Lyapunov exponents as a function of h_x, corresponding to the dashed white line in Fig. 4a, for a fixed value of $\eta = 0.01$ and $\beta_z = 1.0$. The lower color bar in panel (a) indicates the chaotic (**C**, red), periodic (**P**, gray), and quasi-periodic (**QP**, green) dynamical states. Panels (b) and (c) display the winding number as a function of h_x for the selected windows in panel (a). The fixed parameters for these simulations and the initial conditions are the same as those in Fig. 4.

In panel (b) of Fig. 5, we show the results of the calculation of the winding number in the parameter's range $h_x \in [0.6, 1.1]$, and we indeed observe a mix of truly **QP** and phase-locked **QP** states. Recall that the structure of real numbers is such that rational and irrational numbers are deeply intertwined. As a consequence, the winding number exhibits a fractal-like behavior, which is characteristic of quasi-periodic systems. This fact directly affects the values of the winding number, as shown in panel (b) Fig. 5, where one observes the well-known Devil's staircase [51], in which constant winding number $\mathcal{W}$ indicates the regions where the frequency ratio is rational, and the dynamics is periodic. This structure emerges due to the hierarchical embedding of periodic and quasi-periodic states, a phenomenon commonly found in mode-locking scenarios. The fractal character of the staircase is well-known and can be appreciated if one zooms into the structure at several levels of magnification (not shown here).

In panel (c) of Fig. 5, we show the results of calculating the winding number $\mathcal{W}$ in the parameter's range $h_x \in [3.6, 4.4]$. An interesting phenomenon occurs in this range: one observes a more complex double Devil's staircase structure. This phenomenon corresponds to a mode-locking hysteresis. Unlike the standard Devil's staircase, where transitions between locked and quasi-periodic states follow a well-defined order, here we observe overlapping regions of bistability, leading to a hysteresis effect. This mode-locking hysteresis has been reported recently in a different physical system consisting of a spatiotemporal mode-locked laser by Wu et al. [118].

Quantitative information about the dynamics is obtained from the study of the winding number. One interesting observation from the previous analysis is that the different behaviors, i.e., true and locked **QP** states, can also be directly detected in the Lyapunov calculations if they are performed with sufficiently high accuracy. Indeed, the true **QP** states are those exhibiting three vanishing Lyapunov exponents in the studied system.

Fig. 6 presents a detailed color-coded diagram of the winding number $\mathcal{W}$ as a function of both the magnetic field parameter h_x and the damping coefficient η. The color gradient transitions from yellow (indicating lower $\mathcal{W}$ values) to red (denoting higher $\mathcal{W}$ values), illustrating the complex relationship between the magnetic field and damping effects on the system's topological characteristics. In the enlarged region, the interaction between the magnetic field parameters and the damping factor is examined in detail, specifically in the domain previously associated with the manifestation of the devil's staircase in Fig. 5. This closer view reveals a gradual and diffuse transition between quasi-periodic and chaotic states, represented by a subtle fusion of colors on the map, suggesting a complex overlay of underlying dynamics.

In contrast to the well-defined transitions observed in other regions of the study, the devil's staircase appears less sharply here, indicating a complex interaction between different dynamic regimes. The characteristic stepped pattern, typical of the devil's staircase, is blurred in this area, reflecting the close coexistence of periodicity and chaos and the difficulty in clearly distinguishing between these states due to their mutual influence.

This phenomenon highlights the richness and complexity of the magnetization dynamics in the studied system, where slight variations in parameters can trigger significant changes in dynamical behavior. The presence of diffuse transitions between quasi-periodic and chaotic states raises essential considerations for predicting and manipulating magnetic textures, especially in applications requiring high precision and stability, such as reservoir computing.

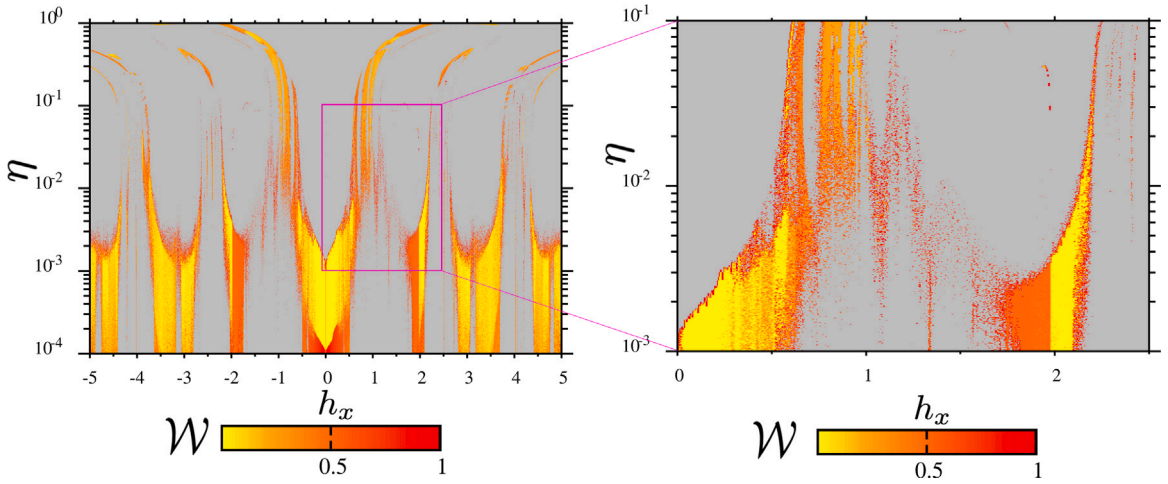

Fig. 6. Phase diagrams in color code of the winding number $\mathcal{W}$ as a function of the magnetic field parameter h_x and the damping coefficient η. The color scale represents the magnitude of $\mathcal{W}$, ranging from yellow for the lowest values to red for the highest, while gray indicates a zero value. The enlarged region highlights the detailed features of the dependence of $\mathcal{W}$ on h_x and η, revealing transitions between different magnetic regimes. The fixed parameters and initial conditions used in these simulations are the same as those in Fig. 4.

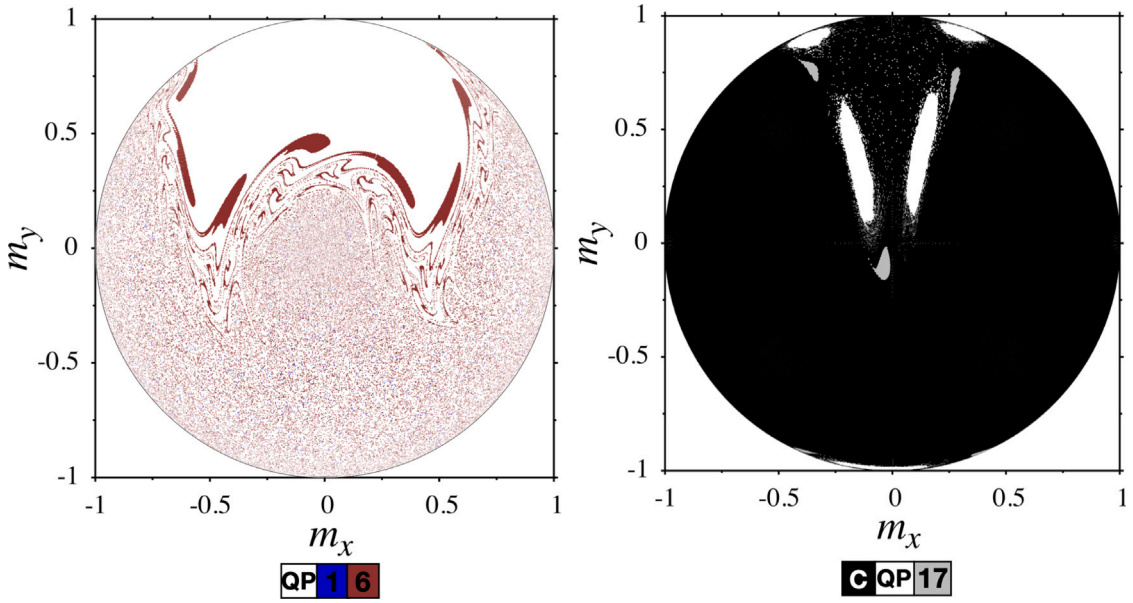

Fig. 7. Diagram of the basin of attraction in the (m_x, m_y) plane, obtained by varying 1×10^6 initial conditions over the sphere at $\eta = 0.01$ for two different values of the magnetic field: $h_x = 0.653$ (left) and $h_x = 2.5$ (right). The remaining parameters are the same as in Fig. 5.

3.5. Effect of initial conditions

Let us finally discuss the effect of initial conditions on the dynamical states, as nonlinear systems can exhibit multistable solutions, some of which are hidden attractors [84,97,119–131]. Indeed, LLG-like equations also display this multiple-stability phenomenon [43,61]. To illustrate this behavior, we compute isospike diagrams as a function of the initial conditions for two different cases previously obtained from the Lyapunov spectrum. In particular, we have selected two specific values of the applied field from Fig. 5, one corresponding to a **QP** state ($h_x = 0.653$) and the other to a chaotic state ($h_x = 2.5$). Fig. 7 displays two diagrams of the basin of attraction in the (m_x, m_y) plane, varying 1×10^6 initial conditions randomly distributed over the sphere. The diagrams allow us to distinguish among periodic, quasi-periodic, and chaotic states using the number of peaks in the time series as an indicator. As in the previous figure, the color code corresponds to the number of peaks, with different colors indicating distinct peak counts, while white points represent quasi-periodic states and black points denote chaotic ones. In the left panel, at $h_x = 0.653$, we observe that only periodic and quasi-periodic states occur, with 84.6% quasi-periodic and 15.4% periodic. For periodic states, only

two types of periodicity are observed: one with six peaks and one with a single peak, the latter being much less likely. Conversely, in the right panel of Fig. 7, at $h_x = 2.5$, we find all three types of states: chaotic, periodic, and quasi-periodic. The vast majority are chaotic, while regular states occur in smaller proportions. Specifically, we have 1.3% periodic states, 4.3% quasi-periodic states, and 94.4% chaotic states. Notably, in this case the number of peaks per period is quite high, reaching up to 17 peaks. This subsection underscores the importance of studying the basins of attraction in multistable systems, particularly in magnetic systems amenable to experimental testing.

4. Final remarks

Recent advancements in nanotechnology have enabled the precise tailoring of magnetic nanoparticle properties, allowing researchers to control key material parameters such as magnetic anisotropy and damping with remarkable accuracy. This progress opens the door to the fabrication of materials with predefined dynamic behaviors suited for specific technological applications. Additionally, the exponential increase in computational power over the past decades has made it feasible to conduct exhaustive parameter-space explorations that were previously computationally prohibitive. In particular, the precise calculation of Lyapunov exponents and other nonlinear dynamical indicators was once an arduous task due to its high computational cost but is now achievable with high precision.

The results presented in this manuscript provide a comprehensive characterization of the dynamical behaviors of an anisotropic magnetic nanoparticle under a time-varying external field. We have identified a rich variety of dynamical regimes, including periodic, quasi-periodic, and chaotic states, mapped out phase diagrams, and analyzed transitions between these states. The emergence of **QP** states and multistability has been systematically studied, offering insights into their fundamental properties and potential experimental validation in future studies.

This study paves the way for designing magnetic nanoparticles with tailored dynamical responses, which could be leveraged for technological applications requiring precise control over magnetization dynamics. However, it is important to note that other material parameters, such as temperature effects and additional interaction terms, were not considered in this study. While these factors are beyond the scope of this work, they could influence the system's behavior and merit further investigation.

Finally, we emphasize that although materials science and dynamical systems are often treated as distinct disciplines, they share fundamental principles. Our findings demonstrate how the interplay between nonlinear dynamics and material properties can lead to complex behaviors, highlighting the importance of interdisciplinary approaches in the study of magnetic nanoparticle dynamics.

CRediT authorship contribution statement

J.A. Vélez: Writing – original draft, Visualization, Software. **L.M. Pérez:** Writing – review & editing, Project administration, Conceptualization. **A.E. Pizarro:** Methodology, Data curation. **L. Pedraja-Rejas:** Visualization, Validation, Formal analysis. **O.J. Suarez:** Visualization, Validation, Formal analysis. **R. Hernández-García:** Methodology, Data curation. **R.J. Barrientos:** Methodology, Data curation. **J. Bragard:** Writing – review & editing, Visualization, Software, Methodology. **D. Laroze:** Writing – review & editing, Writing – original draft, Supervision, Project administration, Conceptualization. **R.M. Otxoa:** Validation, Supervision.

Declaration of competing interest

The authors declare that they have no known competing financial interests or personal relationships that could have appeared to influence the work reported in this paper.

Acknowledgments

LMP acknowledges financial support from ANID through Convocatoria Nacional Subvención a Instalación en la Academia Convocatoria Año 2021, Grant SA77210040. JB acknowledges partial financial support from MINECO (Spain) research project with reference: PID2023-152610OB-C22. RHG acknowledges partial financial support from ANID through FONDECYT 11220693. RJB acknowledges partial financial support from ANID through FONDECYT 1200810. DL acknowledges partial financial support from Centers of Excellence with BASAL/ANID financing, AFB220001, CEDENNA. LMP and DL acknowledges partial financial support from ANID through FONDECYT 1240985. Finally, LMP acknowledges the hospitality of *Universidad de Navarra* (Spain) and *Universidad de Sucre* (Colombia) were part of this work was written.

Appendix A. Winding number computation

As mentioned in the main text, the computation of the winding number is useful for determining the dynamical regime of the system. In particular, irrational winding numbers correspond to quasi-periodic dynamics. In this Appendix, we detail the computation of the winding number using an example, applying different techniques, and relating it to the definition given by the equation:

$$\mathcal{W} = \lim_{i\to\infty} \frac{\theta_i - \theta_0}{2\pi i} \,, \tag{A.1}$$

Note that the 2π factor in the denominator of the above formula serves to normalize the winding number within the interval $[0, 1]$.

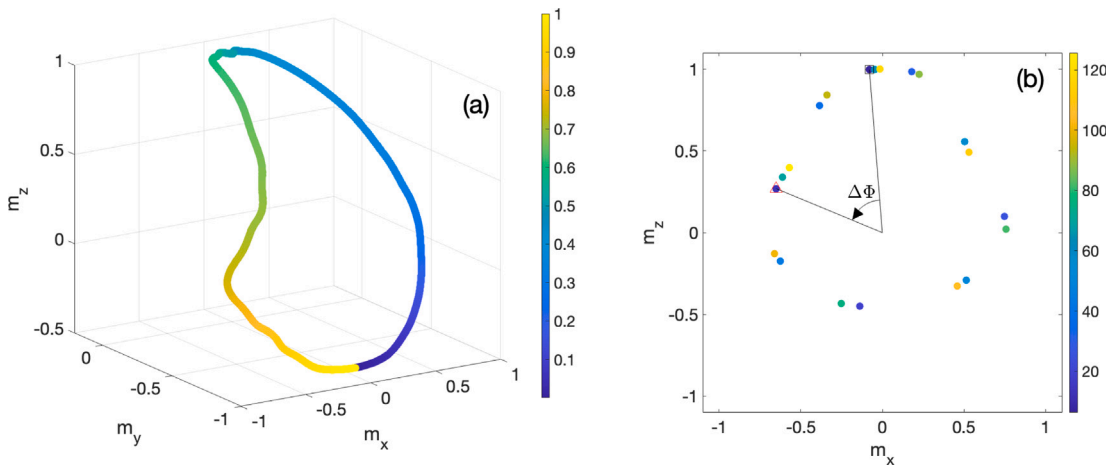

Fig. A.8. Two stroboscopic Poincaré sections. The left panel (a) shows a 3D section in phase space, where the color code represents the normalized curvilinear abscissa along the curve. The right panel (b) presents a 2D projection of the Poincaré section in the (m_x, m_z) plane, displaying a few successive crossing points. In panel (b), the color code of the crossing points corresponds to their successive landing times in the plane. The first point in the series is marked with a black square, while the second is marked with a red triangle. The arrow in panel (b) indicates the phase increment $\Delta\Phi$ between these two successive points. The parameters are set to $h_x = 1$ and $\beta_z = 1$, while the remaining parameters and initial conditions are identical to those in Fig. 5(panel b).

To compute the winding number, the first step consists of defining a stroboscopic Poincaré section, i.e., we record the successive points that land in the Poincaré section after a time interval $\tau_1 = 1/\mathcal{F}_1$. Depending on when the initial point is recorded, the Poincaré section may differ, but the winding number remains invariant. This is illustrated in Fig. A.8. In Fig. A.8a, we present a 3D Poincaré section in phase space. For such a curve in 3D, we compute the curvilinear abscissa, shown with color coding, and normalize it within the range $(0, 1)$. The **QP** dynamics ensures that after each time interval $\tau_1 = 1/\mathcal{F}_1$, the system returns to the curve. If the system is in a **QP** state, the curve is continuous. The winding number is defined as the average of the successive increments of the curvilinear abscissa (modulo one). If the 3D Poincaré section can be projected onto a 2D plane where a unique phase is well-defined, then an alternative method can be used, which is often easier to implement. In Fig. A.8b, each successive visit to the Poincaré section defines a phase increment (modulo 2π). Again, the winding number is given by the average phase increment over multiple visits to the Poincaré section (theoretically taking the limit to infinity). In this case, as seen in Fig. A.8b, we conventionally divide the result by 2π to ensure that the winding number remains within the range $(0, 1)$. Note that the two color bars in Fig. A.8 have completely different meanings. In Fig. A.8a, the color bar represents the 'normalized' curvilinear abscissa on the 3D curve, whereas in Fig. A.8b, it indicates time. Here, each successive point in the 2D section is separated by a constant time interval $\tau_1 = 1/\mathcal{F}_1$.

The accumulation of curvilinear abscissa Δs and phase increments $\Delta\Phi$ are kept for a very long time, respectively referring to Fig. A.8(panel a) and (panel b). Fig. A.9 reports the phase increase ($\in \mathcal{R}$) as a function of the crossing number. Here the simulation is performed on 31,830 crossings of the Poincaré section in order to get an accurate approximation of the winding number $\mathcal{W}$. As expected, the phase increase is well approximated by a linear growth. We use a single parameter fit with the fitting parameter corresponding to the slope of the approximate straight line. In this case, we get the approximate value of $\mathcal{W} \approx 0.220468853$ and a confidence interval (with a 95% of confidence) equals to $[0.220468813, 0.220468893]$. Obviously this is an approximation to the winding number. By repeating the same calculation with the accumulation of the abscissa increments Δs, we can also fit a linear growth to the data and we get the approximate value of $\mathcal{W} \approx 0.2204685516$ and a confidence interval (with a 95% of confidence) equals to $[0.22046854, 0.220468563]$.

A third way to compute an approximation of the winding number is through the use of the Hilbert transform. Indeed, the Hilbert transform is a useful tool to define a phase from a real valued signal. In this case, one select one of the component of the signal, i.e., m_x and we keep the stroboscopic values of m_x. Then we compute the Hilbert transform of this vector. The resulting transform is a complex vector and we can directly compute the phase and compute the phase increment as previously using the *atan*2 function applied on the complex vector. This method gives the approximate value of $\mathcal{W} \approx 0.2204686573$ and a confidence interval (with a 95% of confidence) equals to $[0.2204686379, 0.2204686767]$.

Finally, a fourth way to compute an approximation of the winding number is through the use of the Fourier transform of one of the component of the signal, i.e., m_x. Indeed, it is well known that the spectrum of a quasi-periodic signal possesses a characteristic shape in the Fourier space with a large number of peaks that correspond to the multiples of the two fundamental frequencies of the signal as shown in Fig. A.10. The precision of the method in order to approximate the winding number depends directly from the precision on the computation of the Fourier spectrum. Here the winding number is obtained as the ratio of the two dominant frequencies. We compute $\mathcal{W} = f_2/f_1$. Here we have computed the Fourier spectrum with the FFT of $N = 2^{19}$ sampling points. The sampling time is set to $dt_s = 0.1$, i.e., we sample the dynamics every one hundred numerical time step. With this number of points and this fixed sampling time, the accuracy on the frequency is $\Delta f \approx 1.9 \times 10^{-5}$ and the corresponding accuracy in evaluating the winding number is $\Delta\mathcal{W} \approx 3.5 \times 10^{-5}$. The use of the Fourier method gives an approximate value of $\mathcal{W} \approx 0.2204243$. Though the

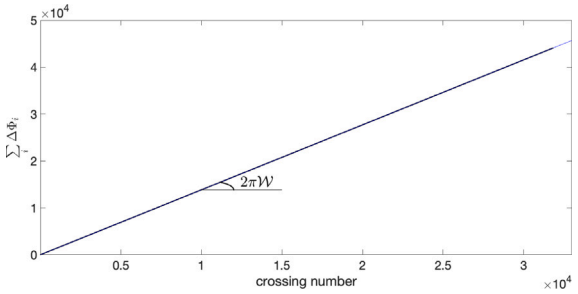

Fig. A.9. The accumulation of the phase increment $\sum(\Delta\Phi)$ exhibits a linear growth with the crossing number in the Poincaré section. The slope of this growth corresponds to the winding number $\mathcal{W}$. In this case, we set $h_x = 1$ and $\beta_z = 0.8$, while the remaining parameters and initial conditions are the same as those in Fig. 5(panel b). For these specific parameters, the computed winding number is $\mathcal{W} \approx 0.220468853$.

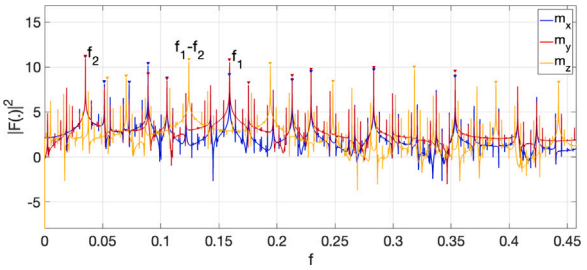

Fig. A.10. Power spectra of the Fourier transforms of the three components of **m**. The dominant frequencies are identified as $f_1 = 1/(2\pi)$ and $f_2 \approx 0.035$. In this case, we set $h_x = 1$ and $\beta_z = 0.8$, while the remaining parameters and initial conditions are the same as those in Fig. 5(panel b).

Table A.2
Summary of the approximate winding number values computed using four different methods for the specific example discussed in the Appendix. The third column presents the standard error (SE) associated with each approximation.

Method	$\mathcal{W}$	S.E.
$\sum(\Delta\Phi)$	0.220468853	10^{-7}
$\sum(\Delta s)$	0.2204685516	10^{-7}
Hilbert	0.2204686573	10^{-7}
Fourier	0.22042	3.510^{-5}

Fourier method is less accurate than the previous methods, it is much simpler to implement in an algorithm. Therefore we have computed the approximated winding number with the Fourier method.

The following table summarizes the results of the computation of the winding number with the four proposed methods (see Table A.2).

Appendix B. Numerical integrators

In this Appendix, we compare the integration of the dynamical Eqs. (1) using two different numerical techniques. For most of the simulations, we employ the standard RK4 scheme with a very small time step (compared to the characteristic time scale of the dynamics), i.e., $d\tau = 0.001$. Additionally, we use a pseudo-symplectic scheme from the Runge–Kutta family, which was recently introduced in the context of incompressible flow with energy conservation [115]. It is well known that the standard RK4 scheme does not exactly conserve phase space volume. This implies that for Hamiltonian systems, where Liouville's theorem holds, the numerical scheme can introduce small perturbations that lead to spurious non-conservative dynamics. In classical mechanics, this issue is typically addressed by employing symplectic integrators, such as the Gauss–Legendre method [116]. However, most symplectic integrators are computationally expensive because they are implicit schemes and require solving a nonlinear equation at each time step. A good trade-off between computational efficiency and accuracy is achieved by using pseudo-symplectic integrators, which are fully explicit. The pseudo-symplectic scheme used in this study is the PSP '4p7q(6)' scheme introduced by Calvo et al. [132]. The nomenclature '4p7q(6)' indicates that the scheme is of order $p = 4$ and preserves kinetic energy to order $q = 7$ using a 6-stage scheme. The corresponding Butcher tableau, which provides the coefficients of the method, can be found in Ref. [115]. This numerical integrator was compared with the classical RK4 scheme, which is a 4-stage scheme, using the same time step $d\tau = 0.001$.

The first aspect we compared was the level of conservation of $|\mathbf{m}| = 1$. Fig. B.11 presents a comparison of the evolution of the modulus $|\mathbf{m}|$ as a function of time over a very long integration period, i.e., 5×10^5. We selected the equation parameters to ensure

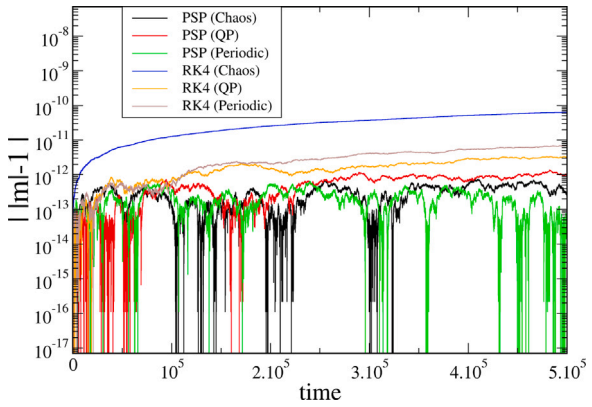

Fig. B.11. The time evolution of $\| \mathbf{m}| - 1|$ is shown for three cases: Periodic, Quasi-Periodic, and Chaotic, using two numerical schemes (RK4 and PSP '4p7q(6)'). The parameters are set to $h_x = 1$, with $\beta_z = -1.8$ (Chaotic), $\beta_z = 0.8$ (**QP**), and $\beta_z = 0.63$ (Periodic). The remaining parameters and initial conditions are the same as in Fig. 5.

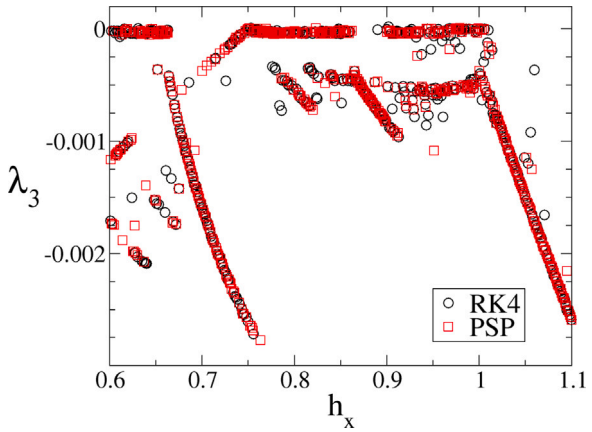

Fig. B.12. The third Lyapunov exponent of the spectrum (λ_3) as a function of the parameter h_x, computed using the standard RK4 scheme (black circles) and the PSP '4p7q(6)' scheme (red squares). This figure is similar to Fig. 5(panel b), but instead of plotting the winding number, it displays λ_3. The remaining parameters and initial conditions are the same as in Fig. 5(panel b), specifically $\eta = 0.01$ and $\beta_z = 1$. The integration time step is set to $d\tau = 0.001$.

the representation of the three typical dynamical regimes: periodic, quasi-periodic, and chaotic. Observing Fig. B.11, we conclude that for the studied dynamics and the chosen time step $d\tau = 0.001$, both numerical integrators yield satisfactory results in terms of magnetization conservation. As expected, the PSP scheme exhibits higher accuracy than the standard RK4 scheme.

As we have extensively used the Lyapunov spectrum in this paper to characterize and differentiate the dynamics, it is necessary to verify the accuracy of the Lyapunov exponent computation with respect to the chosen numerical integrator. It is essential that the results be independent of the numerical integrator. Fig. B.12 displays the computed values of the third Lyapunov exponent (λ_3) as a function of the parameter h_x, obtained using the standard RK4 scheme (black circles) and the PSP '4p7q(6)' scheme (red squares). We observe from Fig. B.12 that the results are very similar, and therefore we can conclude that both schemes are valid for characterizing the dynamics. In particular, a vanishing λ_3 corresponds to **QP** dynamics. However, an important caveat must be noted: the system of Eqs. (1) is sensitive to initial conditions, and thus for some specific parameter values the final state can be extremely sensitive to minute changes, including those introduced by the choice of numerical integrator. Therefore, one cannot expect perfect agreement between the results obtained with the RK4 and PSP schemes, but rather a strong statistical agreement, as clearly shown in Fig. B.12. For reasons of computational efficiency, we performed most of the numerical simulations in this paper using the standard RK4 scheme. We are aware that in some specific applications, where preservation of the Liouville theorem is critical, the pseudo-symplectic scheme would undoubtedly be the integrator of choice.

Data availability

Data will be made available on request.

References

[1] Guo B, Ding S. Landau lifshitz equations. Singapore: World Scientific; 2008.
[2] Gilbert TL. A phenomenological theory of damping in ferromagnetic materials. IEEE Trans Magn 2004;40:3443.
[3] Mayergoyz ID, Bertotti G, Serpico C. Nonlinear magnetization dynamics in nanosystems. North Holland: Elsevier; 2009.
[4] Lakshmanan M. The fascinating world of the Landau-Lifshitz-Gilbert equation: an overview. Phil. Trans R. Soc A. 2011;369:1280–300.
[5] P.E. Wigen, editor. Nonlinear phenomena and chaos in magnetic materials. Singapore: World Scientific; 1994.
[6] Bertotti G, Mayergoyz ID, Serpico C. Identification of the damping coefficient in Landau-Lifshitz equation. Phys B. 2001;306:47.
[7] He P-B, Liu WM. Nonlinear magnetization dynamics in a ferromagnetic nanowire with spin current. Phys Rev B. 2005;72:064410.
[8] Laroze D, Vargas P. Dynamical behavior of two interacting magnetic nanoparticles. Phys B. 2006;372:332.
[9] Laroze D, Vargas P, Cortes C, Gutierrez G. Dynamics of two interacting dipoles. J Magn Magn Mater 2008;320:1440.
[10] Laroze D, Pérez LM. Classical spin dynamics of four interacting magnetic particles on a ring. Phys B. 2008;403:473.
[11] Sementsov DI, Shutyi AM. Nonlinear regular and stochastic dynamics of magnetization in thin-film structures. Phys-Usp 2007;50:793.
[12] Horley PP, Vieira VR, Gorley PM, Dugaev VK, Barnas J. Influence of a periodic magnetic field and spin-polarized current on the magnetic dynamics of a monodomain ferromagnet. Phys Rev B. 2008;77:054427.
[13] Vagin DV, Polyakov P. Control of chaotic and deterministic magnetization dynamics regimes by means of sample shape varying. J Appl Phys 2009;105:033914.
[14] Urzagasti D, Becerra-Alonso D, Pérez LM, Mancini HL, Laroze D. Hyper-chaotic magnetisation dynamics of two interacting dipoles. J Low Temp Phys 2015;181:211.
[15] Laroze D, Becerra-Alonso D, Gallas JAC, Pleiner H. Magnetization dynamics under a quasiperiodic magnetic field. IEEE Trans Magn 2012;48:3567.
[16] Shutyĭ AM, Sementsov DI. Regular and chaotic dynamics of magnetization precession in ferrite-garnet films. Chaos. 2009;;19:013110.
[17] Smith RK, Grabowski M, Camley RE. Period doubling toward chaos in a driven magnetic macrospin. J Magn Magn Mater 2010;322:2127.
[18] Khivintsev Y, Marsh J, Zagorodnii C, Harward I, Lovejoy J, Krivosik P, et al. Nonlinear amplification and mixing of spin waves in a microstrip geometry with metallic ferromagnets. Appl Phys Lett 2011;98:042505.
[19] Shutyi AM, Sementsov DI. Chaotic magnetization dynamics in single-crystal thin-film structures. Crystallogr Rep 2009;54:98.
[20] Khivintsev Y, Kuanr B, Fal TJ, Haftel M, Camley RE, Celinski Z, et al. Nonlinear ferromagnetic resonance in permalloy films: A nonmonotonic power-dependent frequency shift. Phys Rev B. 2010;81:054436.
[21] Laroze D, Bragard J, Suarez OJ, Pleiner H. Characterization of the chaotic magnetic particle dynamics. IEEE Trans Magn 2011;47:3032.
[22] Bragard J, Pleiner H, Suarez OJ, Vargas P, Gallas JAC, Laroze D. Chaotic dynamics of a magnetic nanoparticle. Phys Rev E. 2011;84:037202.
[23] Shutyi AM. Regular and chaotic dynamics of the dipole moment of square dipole arrays. J Exp Theor Phys 2014;118:924.
[24] Phelps MG, Livesey KL, Ferona AM, Camley RE. Tunable transient decay times in nonlinear systems: application to magnetic precession. EPL. 2015;109:37007.
[25] Denisov SI, Lyutyy TV, Pedchenko BO, Hryshko OM. Induced magnetization and power loss for a periodically driven system of ferromagnetic nanoparticles with randomly oriented easy axes. Phys Rev B. 2016;94:024406.
[26] Horley P, Kushnir M, Morales-Meza M, Sukhov A, Rusyn V. Period-doubling bifurcation cascade observed in a ferromagnetic nanoparticle under the action of a spin-polarized current. Phys B: Con. Mat. 2016;486:60.
[27] Clerc MG, Coulibaly S, Laroze D. Nonvariational ising–bloch transition in parametrically driven systems. Int J Bif. Chaos. 2009;19:2717–26.
[28] Pivano A, Dolocan VO. Chaotic dynamics of magnetic domain walls in nanowires. Phys Rev B. 2016;93:144410.
[29] Ferona AM, Camley RE. Nonlinear and chaotic magnetization dynamics near bifurcations of the Landau-Lifshitz-Gilbert equation. Phys Rev B. 2017;95:104421.
[30] Lebrun R, Tsunegi S, Bortolotti P, Kubota H, Jenkins AS, Romera M, et al. Mutual synchronization of spin torque nano- oscillators through a long-range and tunable electrical coupling scheme. Nat Commun 2017;8:15825.
[31] Okano G, Nozaki Y. Evaluation of the effective potential barrier height in nonlinear magnetization dynamics excited by ac magnetic field. Phys Rev B. 2018;97:014435.
[32] Cabanas AM, Pérez LM, Laroze D. Strange non-chaotic attractors in spin valve systems. J Magn Magn Mater 2018;460:320–6.
[33] Diaz P, Laroze D. Configurational temperature for interacting anisotropic magnetic particles. Int. J Bif. Chaos. 2009;19:3485–98.
[34] Gibson C, Bildstein S, Lee JA, Grabowski M. Nonlinear resonances and transitions to chaotic dynamics of a driven magnetic moment. J Magn Magn Mater 2020;501:166352.
[35] Montoya E, Perna S, Chen Y, Katine JA, d'Aquino M, Serpico C, et al. Magnetization reversal driven by low dimensional chaos in a nanoscale ferromagnet. Nat Commun 2019;10:543.
[36] Pérez LM, Bragard J, Mancini HL, Gallas JAC, Cabanas AM, Suarez OJ, et al. Anisotropy effects on magnetization dynamics. Net. Het. Med 2015;10:209.
[37] Ferona AM, Camley RE. Nonlinear power-dependent effects in exchange-coupled magnetic bilayers. Phys Rev B. 2019;99:064405.
[38] Williame J, Accioly AD, Rontani D, Sciamanna M, Kim J. Chaotic dynamics in a macrospin spin-torque nano-oscillator with delayed feedback. Appl Phys Lett 2019;114:232405.
[39] Devolder T, Rontani D, Petit-Watelot S, Bouzehouane K, Andrieu S, Letang J, et al. Chaos in magnetic nanocontact vortex oscillators. Phys Rev Lett 2019;123:147701.
[40] Laroze D, Pérez LM. Classical spin dynamics of four interacting magnetic particles on a ring. Phys B. 2008;403:473–7.
[41] Clerc MG, Coulibaly S, Laroze D. Localized states and non-variational Ising–Bloch transition of a parametrically driven easy-plane ferromagnetic wire. Phys D. 2010;239:72–86.
[42] Clerc MG, Coulibaly S, Laroze D. Localized states beyond the asymptotic parametrically driven amplitude equation. Phys Rev E. 2008;77:056209.
[43] Vélez JA, Bragard J, Pérez LM, Cabanas AM, Suarez OJ, Laroze D, et al. Periodicity characterization of the nonlinear magnetization dynamics. Chaos. 2020;30:093112.
[44] Bragard J, Vélez JA, Riquelme JA, Pérez LM, Hernández-García R, Barrientos RJ, et al. Study of type-III intermittency in the Landau-Lifshitz-Gilbert equation. Phys Scr 2021;96:124045.
[45] Taniguchi T. Chaotic magnetization dynamics driven by feedback magnetic field. Phys Rev B 2024;109:214412.
[46] Berge P, Pomeau Y, Vidal C. Order within chaos: towards a deterministic approach to turbulence. Wiley-VCH; 1987.
[47] Ruelle D, Takens F. On the nature of turbulence. Com. Math Phys 1971;20:167.
[48] Newhouse S, Ruelle D, Takens F. Occurrence of strange axiom a attractors near quasi periodic flows on tm, m is greater than or equal to 3. Commun Math Physic. 1978;64:35.
[49] Kaneko K. Period-doubling of kink-antikink patterns, quasiperiodicity in antiferro-like structures and spatial intermittency in coupled logistic lattice: Towards a prelude of a field theory of chaos. Prog Theor Phys 1984;72:480–6.
[50] Grebogi C, Ott E, Yorke JA. Attractors on an n-torus: quasiperiodicity versus chaos. Phys D. 1985;15:354–73.
[51] Glazier JA, Libchaber A. Quasi-periodicity and dynamical systems: An experimentalist's view. IEEE Trans Circ Syst 1988;35:790.
[52] Tang S, Liu JM. Chaotic pulsing and quasi-periodic route to chaos in a semiconductor laser with delayed opto-electronic feedback. IEEE J Quantum Electron 2001;37(3):329–36.

[53] Deissler RJ, Brand HR. Periodic, quasi-periodic, and chaotic localized solutions of the quintic complex Ginzburg-Landau equation. Phys Rev Lett 1994;72(4):478–81.
[54] Poschel J. Quasi-periodic solutions for a nonlinear wave equation. Comment Math Helv 1996;71(2):269–96.
[55] Noid DW, Koszykowski ML, Marcus RA. Quasi-periodic and stochastic-behavior in molecules. Annu Rev Phys Chem 1981;32:267–309.
[56] Stella L, Vietri M. Lense-thirring precession and quasi-periodic oscillations in low-mass X-ray binaries. Astrophys J 1998;492(1):L59–62.
[57] Barrio R, Rodriguez M, Serrano S, Shilnikov A. Mechanism of quasi-periodic lag jitter in bursting rhythms by a neuronal network. Europhys Lett 2015;112(3):38002.
[58] Garfinkel A, et al. Quasiperiodicity and chaos in cardiac fibrillation. J Clin Invest 1997;99(305).
[59] Clerc MG, Coullet P, Vandenberghe N, Tirapegui R. Quasi-reversible instabilities of closed orbits. Phys Lett A. 2001;287:198–204.
[60] Clerc MG, Verschueren N. Quasiperiodicity route to spatiotemporal chaos in one-dimensional pattern-forming systems. Phys Rev E. 2013;88:052916.
[61] Alvarez LF, Pla O, Chubykalo O. Quasiperiodicity, bistability, and chaos in the Landau-Lifshitz equation. Phys Rev B 2000;61:11613.
[62] Bertotti G, Serpico C, Mayergoyz ID. Nonlinear magnetization dynamics under circularly polarized field. Phys Rev Lett 2001;86:724.
[63] Bertotti G, Magni A, Mayergoyz ID, Serpico C. Bifurcation analysis of Landau-Lifshitz-Gilbert dynamics under circularly polarized field. J Appl Phys 2001;89:6710.
[64] Serpico C, d'Aquino M, Bertotti G, Mayergoyz ID. Analysis of quasiperiodic Landau-Lifshitz-Gilbert dynamics. J Magn Magn Mater 2004;;272–276:734–5.
[65] Petit-Watelot S, Kim JV, Ruotolo A, Otxoa RM, Bouzehouane K, Grollier J, et al. Commensurability and chaos in magnetic vortex oscillations. Nat Phys 2012;8:682–7.
[66] Zolfagharinejad M, Alegre-Ibarra U, Chen T, Kinge S, van der Wiel WG. Brain-inspired computing systems: a systematic literature review. Eur Phys J B. 2024;97:70.
[67] Yamaguchi T, Tsunegi S, Nakajima K, Taniguchi T. Computational capability for physical reservoir computing using a spin-torque oscillator with two free layers. Phys Rev B 2023;107:054406.
[68] Shougat MREU, Perkins E. The van der pol physical reservoir computer. Neuromorphic Comput Eng 2023;3:024004.
[69] Racca A, Magri L. Robust optimization and validation of echo state networks for learning chaotic dynamics. Neural Networks 2021;142:252–68.
[70] Millet L, Jeon H, Kim B, Bhoi B, Kim S-K. Reservoir computing using photon-magnon coupling. Appl Phys Lett 2021;119:182405.
[71] Govia LCG, Ribeill GJ, Rowlands GE, Krovi HK, Ohki TA. Quantum reservoir computing with a single nonlinear oscillator. Phys Rev Res 2021;3:013077.
[72] Tsunegi S, Taniguchi T, Nakajima K, Miwa S, Yakushiji K, Fukushima A, et al. Physical reservoir computing based on spin torque oscillator with forced synchronization. Appl Phys Lett 2019;114:164101.
[73] Kondrashov AV, Nikitin AA, Nikitin AA, Kostylev M, Ustinov AB. Numerical simulation of performance of magnonic reservoir computer based on active-ring oscillator. J Magn Magn Mater 2022;563:169968.
[74] Shougat MREU, Li X, Perkins E. Multiplex-free physical reservoir computing with an adaptive oscillator. Phys Rev E. 2024;109:024203.
[75] Imai Y, Nakajima K, Tsunegi S, Taniguchi T. Input-driven chaotic dynamics in vortex spin-torque oscillator. Sci Rep 2022;12:21651.
[76] Vélez JA, Lee M-K, Tatara G, Gavriloaeea P-I, Ross J, Laroze D, et al. Chaotic proliferation of relativistic domain walls for reservoir computing. 2024, arXiv. 2412.20308.
[77] Beaurepaire E, Merle JC, Daunois A, Bigot JY. Ultrafast spin dynamics in ferromagnetic nickel. Phys Rev Lett 1996;76:4250.
[78] Hubert A, Schafer RMagnetic Domains. The analysis of magnetic microstructures. Berlin-Heidelberg: Springer-Verlag; 1998.
[79] Coey JMD. Magnetism and magnetic materials. Cambridge: Cambridge University Press; 2009.
[80] Zhao Y, Song Q, Yang S-H, Su T, Yuan W, Parkin SSP, et al. Experimental investigation of temperature-dependent gilbert damping in permalloy thin films. Sci Rep 2016;6:22890.
[81] Oogane M, Wakitani T, Yakata S, Yilgin R, Ando Y, Sakuma A, et al. Magnetic damping in ferromagnetic thin films. Japan J Appl Phys 2006;45(5A):3889–91.
[82] Kumar A, Pan F, Husain S, Akansel S, Brucas R, Bergqvist L, et al. Temperature-dependent Gilbert damping of Co_2MnSi thin films with different degree of atomic order. Phys Rev B. 96(22):224425.
[83] Wolf A, Swift JB, Swinney HL, Vastano JA. Determining Lyapunov exponents from a time series. Phys D. 1985;16:285.
[84] Sprott JC. Chaos and time-series analysis. UK: Oxford University Press; 2003.
[85] Boccaletti S, Grebogi C, Lai YC, Mancini H, Maza D. The control of chaos: theory and applications. Phys Rep 2000;329:103–97.
[86] Boccaletti S, Valladares DL, Kurths, Maza D, Mancini H. Synchronization of chaotic structurally nonequivalent systems. Phys Rev E. 2000;61:3712.
[87] Barrio R, Serrano S. A three-parametric study of the Lorenz model. Phys D: Nonlinear Phenom 2007;229:43.
[88] Dullin HR, Schmidt S, Richter PH, Grossmann SK. Extended phase diagram of the Lorenz model. Int J Bifurc Chaos. 2007;17:3013.
[89] Barrio R, Blesa F, S. Serrano. Periodic, escape and chaotic orbits in the copenhagen and the (n+ 1)-body ring problems. Commun Nonlinear Sci Numer Simul 2009;14(5):2229–38.
[90] Barrio R, Borczyk W, Breiter R. Spurious structures in chaos indicators maps. Chaos Solitons Fractals 2009;40(4):1697–714.
[91] Park J, Lee H, Jeon Y, Bai J. Periodicity of the lorenz-stenflo equations. Phys Scr 2015;90:065201.
[92] Laroze D, Pleiner H. Thermal convection in a nonlinear non-newtonian magnetic fluid. Commun Nonlinear Sci Numer Simul 2015;26:167.
[93] Fazanaro FI, Soriano DC, Suyama R, Madrid MK, de Oliveira JR, Bravo Muñoz I, et al. Numerical characterization of nonlinear dynamical systems using parallel computing: The role of GPUs approach. Commun Nonlinear Sci Numer Simul 2016;37:143.
[94] Park J, Lee H, Baik J. Periodic and chaotic dynamics of the ehrhard-müller system. Int J Bif. Chaos. 2016;26:1630015.
[95] Gallas JAC. Spiking systematics in some CO2 laser models. Adv At Mol Opt Phys 2016;65:127–91.
[96] Moon S, Han B, Park J, Seo JM, Baik J. Periodicity and chaos of high-order Lorenz systems. Int J Bif. Chaos. 2017;27:1750176.
[97] Wiggers V, Rech PC. Multistability and organization of periodicity in a Van der Pol-Duffing oscillator. Chaos, Sol Fra 2017;103:632–7.
[98] Pikovsky A, Politi A. Lyapunov exponents: a tool to explore complex dynamics. Cambridge U. Press; 2016.
[99] Ramírez G, Jánosi IM, Gallas JAC. Two-parameter areal scaling in the Hénon map. Europhys Lett 2019;126:20001.
[100] Freire JG, Caldeórn A, Varela H, Gallas JA. Phase diagrams and dynamical evolution of the triple-pathway electro-oxidation of formic acid on platinum. Phys Chem Chem Phys 2020;22:1078–91.
[101] Mahmud MN, Siri Z, Vélez JA, Pérez LM, Laroze D. Chaotic convection in an oldroyd viscoelastic fluid in saturated porous medium with feedback control. Chaos. 2020;30:073109.
[102] Gallas JAC. Stability diagrams for a memristor oscillator. Eur Phy. J Spe. Top 2019;228:2081.
[103] Barrio R, Blesa F, Serrano S. Topological changes in periodicity hubs of dissipative systems. Phy. Rev Lett 2012;108:214102.
[104] Barrio R, Martínez MA, Serrano S, Wilczak D. When chaos meets hyperchaos: 4D rössler model. Phys Lett A. 2015;379:2300.
[105] Wilczak D, Serrano S, Barrio R. Coexistence and dynamical connections between hyperchaos and chaos in the 4D Rössler system: A computer-assisted proof. SIAM J Appl Dyn Syst 2016;15:356.
[106] Barrio R, Ibáñez S, Pérez L, Serrano S. Spike-adding structure in fold/hom bursters. Commun Nonlinear Sci Numer Simul 2020;83:105100.
[107] Barrio R, Lozano A, Rodriguez M, Serrano S. Numerical detection of patterns in CPGs: Gait patterns in insect movement. Commun Nonlinear Sci Numer Simul 2020;82:105047.
[108] Barrio R, Coombes S, Desroches M, Fenton F, Luther S, Pueyo E. Excitable dynamics in neural and cardiac systems. Commun Nonlinear Sci Numer Simul 2020;86:105275.

[109] Rao X-B, Zhao X-P, Gao J-S, Zhang J-G. Self-organizations with fast-slow time scale in a memristor-based Shinriki's circuit. Commun Nonlinear Sci Numer Simul 2021;94:105569.
[110] Kanchana C, Vélez JA, Pérez LM, Laroze D, Siddheshwar PG. Influence of higher-order modes on ferroconvection. Chaos 2022;32:083129.
[111] Pérez LM, Vélez JA, Mahmud MN, Corona RM, Castillo-Sepúlveda S, Pedraja-Rejas L, et al. Complexity measurements for the thermal convection in a viscoelastic fluid saturated porous medium. Results Phys 2023;52:106737.
[112] Siddheshwar PG, Kanchana C, Pérez LM, Laroze D. Influence of symmetric/asymmetric boundaries on axisymmetric convection in a cylindrical enclosure in the presence of a weak vertical throughflow. Commun Nonlinear Sci Numer Simul 2023;126:107495.
[113] Garai S, Karmakar S, Jafari S, Pal N. Coexistence of triple, quadruple attractors and wada basin boundaries in a predator–prey model with additional food for predators. Commun Nonlinear Sci Numer Simul 2023;121:107208.
[114] Reyes LI, Pérez LM, Pedraja-Rejas L, Díaz P, Mendoza J, Bragard J, et al. Characterization of faraday patterns and spatiotemporal chaos in parametrically driven dissipative systems. Chaos Solitons Fractals 2024;186:115244.
[115] Capuano F, Coppola G. Explicit Runge–Kutta schemes for incompressible flow with improved energy-conservation properties. J Comput Phys 2017;328:86–94.
[116] Botha AE, M. Shukrinov Yu, Tekić J, Kolahchi MR. Chaotic dynamics from coupled magnetic monodomain and josephson current. Phys Rev E 2023;107:024205.
[117] Wolfgang MS. Diophantine approximations and diophantine equations. Heidelberg: Lecture Notes in Mathematics; 1991.
[118] Wu H, Lin W, Tan Y-J, Cui H, Luo Z-C, Xu W-C, et al. Pulses with switchable wavelengths and hysteresis in an all-fiber spatio-temporal mode-locked laser. Appl Phys Express. 2020;13:022008.
[119] Sambas A, Vaidyanathan S, Tlelo-Cuautle E, Abd-El-Atty B, El-Latif AAABD, Guillén-Fernández O, et al. A 3-D multi-stable system with a peanut-shaped equilibrium curve: Circuit design, FPGA realization, and an application to image encryption. IEEE Access 2020;8:137116.
[120] Vaidyanathan S, Shaobo H, Sambas A. A new multistable double-scroll 4-D hyperchaotic system with no equilibrium point, its bifurcation analysis, synchronization and circuit design. Arch Control Sci 2021;31:99.
[121] Rech PC, Dhua S, Pati NC. Multistability and bubbling route to chaos in a deterministic model for geomagnetic field reversals. Int J Bif. Chaos. 2019;29:1930034.
[122] Bayani A, Rajagopal K, Khalaf AJM, Jafari S, Leutcho GD, Kengne J. Dynamical analysis of a new multistable chaotic system with hidden attractor: Antimonotonicity, coexisting, multiple attractors, and offset boosting. Phys Lett A 2019;383:1450.
[123] Cabanas AM, Rivas R, Pérez LM, Vélez J, Díaz P, Clerc MG, et al. Malomed: A quasi-periodic route to chaos in a parametrically driven nonlinear medium. Chaos Solit. Fractals 2021;151:111089.
[124] Wei Z, Pham V-T, Khalaf AJM, Kengne J, Jafari S. A modified multistable chaotic oscillator. Int J Bifurcat. Chaos 2018;28:1850085.
[125] Pisarchik AN, Feudel U. Control of multistability. Phys Rep 2014;540:167.
[126] Dudkowski D, Jafari S, Kapitaniak T, Kuznetsov NV, Leonov GA, Prasad A. Hidden attractors in dynamical systems. Phys Rep 2016;637:1.
[127] Jafari S, Sprott JC, Nazarimehr F. Recent new examples of hidden attractors. Eur Phys J Spec. Top 2015;224:1469.
[128] Siddheshwar PG, Kanchana C, D Larozem. A study of Darcy-Bénard regular and chaotic convection using a new local thermal non-equilibrium formulation. Phys Fluids 2021;33:044107.
[129] Munmuangsaen B, Srisuchinwong B. A hidden chaotic attractor in the classical lorenz system. Chaos, Sol Fra. 2018;107:61.
[130] Chen Z, Zhao H. Self-similar attractor sets of the lorenz model in parameter space. Chaos Solit. Fractals 2023;173:113651.
[131] Valani RN. Infinite-memory classical wave-particle entities, attractor-driven active particles, and the diffusionless lorenz equations. Chaos 2024;34:013133.
[132] Calvo M, Laburta M, Montijano J, Rández L. Approximate preservation of quadratic first integrals by explicit Runge–Kutta methods. Adv Comput Math 2010;32:255–74.